Title
Stepwise assembly of heterobimetallic complexes: synthesis, structure, and physical properties

Journal
Dalton Transactions, 50(23)

ISSN
1477-9226

Authors
Lee, Justin L
Oswald, Victoria F
Biswas, Saborni
et al.

Publication Date
2021-06-15

DOI
10.1039/d1dt01021b

Peer reviewed

HHS Public Access

Author manuscript

Dalton Trans. Author manuscript; available in PMC 2021 September 05.

Published in final edited form as:

Dalton Trans. 2021 June 15; 50(23): 8111–8119. doi:10.1039/d1dt01021b.

Stepwise assembly of heterobimetallic complexes: synthesis, structure, and physical properties†

Justin L. Lee[a], **Victoria F. Oswald**[a], **Saborni Biswas**[b], **Ethan A. Hill**[a], **Joseph W. Ziller**[a], **Michael P. Hendrich**[b], **A. S. Borovik**[a]

[a]Department of Chemistry, 1102 Natural Sciences II, University of California, Irvine, California 92697, USA.

[b]Department of Chemistry, Carnegie Mellon University, 4400 Fifth Avenue, Pittsburgh, Pennsylvania 15213, USA

Abstract

Bimetallic active sites are ubiquitous in metalloenzymes and have sparked investigations of synthetic models to aid in the establishment of structure–function relationship. We previously reported a series of discrete bimetallic complexes with [Fe^{III}–(μ-OH)–M^{II}] cores in which the ligand framework provides distinct binding sites for two metal centers. The formation of these complexes relied on a stepwise synthetic approach in which an Fe^{III}–OH complex containing a sulfonamido tripodal ligand served as a synthon that promoted assembly. We have utilized this approach in the present study to produce a new series of bimetallic complexes with [Fe^{III}–(μ-OH)–M^{II}] cores (M = Ni, Cu, Zn) by using an ancillary ligand to the Fe^{III} center that contains phosphinic amido groups. Assembly began with formation of an Fe^{III}–OH that was subsequently used to bind the M^{II} fragment that contained a triazacyclononane ligand. The series of bimetallic complexes were charactered structurally by X-ray diffraction methods, spectroscopically by absorption, vibrational, electron paramagnetic resonance spectroscopies, and electrochemically by cyclic voltammetry. A notable finding is that these new [Fe^{III}–(μ-OH)–M^{II}] complexes displayed significantly lower reduction potentials than their sulfonamido counterparts, which paves way for future studies on high valent bimetallic complexes in this scaffold.

Introduction

Complexes with discrete bimetallic cores are found in a number of biological and synthetic systems and have impact on both physical and functional properties.[1-4] Within a biological context, chemical transformations are often regulated by the cooperative effects of bimetallic cores in which each metal center usually has a different primary coordination sphere.[5-13] Replicating these structural features within synthetic systems has been difficult because

†Electronic supplementary information (ESI) available: Tables S1 and S2 and Fig. S1-S3, details of EPR simulation, and crystallographic data in CIF format. CCDC 2072600–2072603. For ESI and crystallographic data in CIF or other electronic format see DOI: 10.1039/d1dt01021b

aborovik@uci.edu .

Conflicts of interest

There are no conflicts to declare.

many preparative methods lead to each metal center having identical sets of ligand donors.[14-23] These methodological restrictions also hinder the preparation of complexes in which the bimetallic cores contain different metal ions.[24-26] One approach to circumvent these problems is to design a metal complex with an auxiliary binding site that can bind an additional, and different, metal complex.[27-36] Notable examples that use this approach are the heterobimetallic complexes of Thomas and Lu who have designed ligands that promote formation of complexes with M–M′ bonds.[37-42]

We are developing a different approach for the stepwise assembly of heterobimetallic complexes that produces systems with [Fe^{III}–(μ-OH)–M^{II}] cores. The general design uses a monomeric Fe^{III}–OH synthon that contains a tripodal ligand with three structural characteristics: (1) it contains a trianionic, tetradentate binding site for the Fe^{III}–OH unit, (2) it contains scaffolding to append hydrogen bond (H–bond) acceptors to form intramolecular H-bonds with the Fe^{III}–OH unit, and (3) it contains an auxiliary metal binding site that includes the hydroxido ligand.[43] These design principles were illustrated in our use of the tripodal ligand $[MST]^{3-}$ (*N,N′,N″*-[2,2′,2″-nitrilotris(ethane-2,1-diyl)]tris(2,4,6-trimethylbenzenesulfonamido), Fig. 1A) that contains three deprotonated sulfonamide groups[44] and was used to prepare a variety of different complexes with [Fe^{III}–(μ-OH)–M^{II}] cores (Fig. 1B).[45-47] We recently introduced a tripodal ligand $[poat]^{3-}$ (*N,N′,N″*-[nitrilotris (ethane-2,1-diyl)]tris(*P,P*-diphenylphosphinic amido)) that instead of sulfonamido groups contains phosphinic amido groups (Fig. 1C).[48] We reasoned that the similarities in the structures of the two tripodal ligands would prepare the analogous [Fe^{III}–(μ-OH)–M^{II}] complexes to compare their properties. We now report our findings for a series of [(TMTACN)M^{II}–(μ-OH)–Fe^{III}poat]$^+$ (M^{II} = Zn, Cu, Ni; TMTACN = 1,4,7-trimethyl-1,4,7-triazacyclononane) complexes that show these types of complexes can be readily assembled to form discrete heterobimetallic complexes. Although they have similar structural and physical properties, the complexes with $[poat]^{3-}$ have significantly lower redox potentials than their sulfonamido counterparts.

Results and discussion

Preparation route for K[Fe^{III}poat(OH)]

The first-step into the assembly of heterobimetallic complexes was to prepare the monomeric synthon [Fe^{III}poat(OH)]$^-$ which was isolated as its potassium salt by addition of one equiv. of O_2 to K[Fe^{II}poat] (Scheme 1).[48] We also found an alternative route using K_2[Fe^{II}poat(OH)] which was prepared from K[Fe^{II}poat] and water (see Experimental section for details): treating this Fe^{II}–OH complex with 0.5 equiv. of I_2 afforded K[Fe^{III}poat(OH)] (Scheme 1). Recrystallization of K[Fe^{III}poat(OH)] from methylene chloride/diethyl ether produced dark yellow crystals in yields of 35%. The molecular structure of [Fe^{III}poat(OH)]$^-$ was determined by X-ray diffraction methods. The salt crystallized as a cluster with two anions of [Fe^{III}poat(OH)]$^-$ bounded to two potassium ions (Fig. 2A, Table S2†). The Fe^{III} center incorporated an exogenous hydroxido ligand in

†Electronic supplementary information (ESI) available: Tables S1 and S2 and Fig. S1-S3, details of EPR simulation, and crystallographic data in CIF format. CCDC 2072600–2072603. For ESI and crystallographic data in CIF or other electronic format see DOI: 10.1039/d1dt01021b

an axial coordination site (Fig. 2B), and the complex had an overall trigonal bipyramidal (tbp) coordination geometry with a trigonality structural parameter (τ_5) value of 0.948 (the ideal trigonal bipyramidal geometry has a $\tau_5 = 1$, and the ideal square pyramidal geometry has a $\tau_5 = 0$). The crystallization as a cluster prevented intramolecular hydrogen bonds to be formed between the hydroxido ligand and the P═O group of $[poat]^{3-}$. $K[Fe^{III}poat(OH)]$ was treated with 18-crown-6 to increase solubility and exhibited an optical spectrum with a feature at λ_{max} (ε, M^{-1} cm^{-1}) = 370 nm (3800), similar to other mononuclear Fe^{III}–hydroxido complexes in tbp geometry.[47,49-51] The electron paramagnetic resonance (EPR) spectrum of $K[^{57}Fe^{III}poat(OH)]$/18-crown-6 in DMF : THF had features at $g = 4.3$ and 9.6 (Fig. S1A†). Additionally, the Mössbauer spectrum of $[^{57}Fe^{III}poat(OH)]^-$ showed a six-line pattern consistent with a high-spin Fe^{III} center with an isomer shift (δ) of 0.32 mm s^{-1} and a quadrupole splitting (ΔE_Q) of 0.92 mm s^{-1} (Fig. S1B†). Both magnetic measurements supported a ground spin state assignment of $S = 5/2$.

Preparation route for the [(TMTACN)M^{II}–(μ-OH)–Fe^{III}poat]OTf

The preparation of the discrete heterobimetallic complexes [(TMTACN)M^{II}–(μ-OH)–Fe^{III}poat]OTf (M^{II} = Zn, Cu, Ni and denoted $[M^{II}(OH)Fe^{III}]^+$) was achieved *via* the preparative route outlined in Scheme 2. In a typical reaction, NMe_4OAc was added to a CH_2Cl_2 solution of $K[Fe^{III}poat(OH)]$, and after removal of the insoluble KOAc, the resulting mixture was treated with the appropriate $[M^{II}(TMTACN)]^{2+}$ complex. $[Zn^{II}(TMTACN)(OTf)_2]$ and $[Cu^{II}(TMTACN)(OTf)_2]\cdot CH_3CN$[52] salts were used to synthesize the $[Zn^{II}(OH)Fe^{III}]^+$ and $[Cu^{II}(OH)Fe^{III}]^+$ species; however, attempts to synthesize and isolate $[Ni^{II}(TMTACN)(OTf)_2]$ in high purity had been unsuccessful, which led to this salt being generated *in situ* by mixing equimolar of $Ni^{II}(OTf)_2\cdot 5CH_3CN$ and TMTACN in CH_2Cl_2. The $[M^{II}(OH)Fe^{III}]$OTf salts were first purified as powders *via* precipitation from diethyl ether–CH_2Cl_2 mixtures, and were then further purified *via* recrystallization as yellow sheet-like crystals from pentane (or hexane)–CH_2Cl_2 mixtures. These crystals were suitable for single crystal X-ray diffraction measurements, elemental analysis, and additional characterization methods. The formulations of the $[M^{II}(OH)Fe^{III}]^+$ complexes were supported by ESI-MS, in which the *m/z* values and experimental isotope patterns matched those calculated for $[M^{II}(OH)Fe^{III}]^+$ (Fig. 3). The three complexes have similar optical properties with absorbance features around λ_{max} = 315, 372, and 460 nm (Fig. 4, S2†). In particular, the absorbance feature with a λ_{max} = 372 nm is similar to those previously reported in our related heterobimetallic complexes with the $[MST]^{3-}$ ligand.[46]

Vibrational properties of $[M^{II}(OH)Fe^{III}]^+$ complexes

Solid-state vibrational properties of the $[M^{II}(OH)Fe^{III}]^+$ compounds were investigated by FTIR spectroscopy and exhibit similar features (Fig. S3†). For example, the vibrational spectrum of $[Zn^{II}(OH)Fe^{III}]$OTf revealed a weak vibrational feature at 3141 cm^{-1} that is assigned to the ν(O–H) band. This energy is lower, and the peak is broader than the corresponding ν(O–H) feature observed in the analogous complex with the $[MST]^{3-}$ ligand, which appears at an energy of 3238 cm^{-1}.[46] These observations are consistent with the phosphinic amido P═O group in $[poat]^{3-}$ being a stronger H-bond acceptor than the sulfonamido S═O group in $[MST]^{3-}$. For $[Ni^{II}(OH)Fe^{III}]^+$, the ν(O–H) band is at 3160 cm^{-1} and it is similarly broad to suggest that the hydroxido ligand is involved in H-bond

formation. We were unable to detect the ν(O–H) feature in the $[Cu^{II}(OH)Fe^{III}]^{+}$ which could be attributed to the relatively lower Lewis acidity of Cu^{II} ion,[53] and that would strengthen the H-bond and broaden any ν(O–H) feature. The remaining portion of the vibrational spectra of the three complexes are nearly identical, implying that the overall solid-state structures for the three complexes could be similar.

Solid-state molecular structures of $[M^{II}(OH)Fe^{III}]^{+}$ complexes

The molecular structures of the $[M^{II}(OH)Fe^{III}]^{+}$ complexes were determined by X-ray diffraction methods and revealed discrete bimetallic core structures (Fig. 5). There are two crystallographically different, but chemically equivalent, molecules in the asymmetric unit and we will discuss the averages of the metrical parameters and calculated values, which are shown in Table 1. The triflate counter anion is outer-sphere and not interacting with the complex. The Fe^{III} site adopts a similar tbp geometry as found in $[Fe^{III}poat(OH)]^{-}$ with an N_4O primary coordination sphere, comprising of the $[poat]^{3-}$ ligand and the hydroxido ligand. The complexes have τ_5 values ranging 0.877 to 0.885, which are less than that found in $[Fe^{III}poat(OH)]^{-}$ (see above). The Fe1–O1 bond distances are statistically identical within the series (1.887(4)–1.900(2) Å), and are comparable with those previously reported in $[(TMTACN)M^{II}–(\mu\text{-}OH)–Fe^{III}MST]^{+}$ (1.884(2) to 1.892(5) Å).[46]

The M^{II} sites in the series are all 6-coordinated with N_3O_3 primary coordination spheres that are comprised of the TMTACN ligand, two O-atom donors from the phosphinic amido groups of $[poat]^{3-}$, and the bridging hydroxido ligand. A Jahn-Teller distortion is observed in the Cu^{II} site of $[Cu^{II}(OH)Fe^{III}]^{+}$, in which the axial Cu1–O3 and Cu1–N7 bond distances are significantly elongated, while the equatorial Cu1–O1/Cu1–O4/Cu1–N5/Cu1–N6 bond distances are contracted in comparison with those observed in the Zn^{II} and Ni^{II} analogues (Table 1). We note that a similar Jahn–Teller distortion was also observed in the $[(TMTACN)Cu^{II}–(\mu\text{-}OH)–Fe^{III}MST]^{+}$ complex.[46]

We further examined the M^{II}–O═P and $M^{II}–N_{TMTACN}$ bonds in the $[M^{II}(OH)Fe^{III}]^{+}$ complex series; the Cu^{II} analogue is excluded from this discussion because of the aforementioned Jahn–Teller distortion (see above). The M^{II}–O═P bond distances range between 2.089(4)–2.115(2) Å; these values are significantly smaller than the corresponding M^{II}–O(S) bond distances observed in the sulfonamido complexes that range from 2.148(2)–2.362(3) Å.[46] The difference in M^{II}–O bond lengths suggests the phosphinic amido P═O groups are stronger donating ligands than the sulfonamide S═O groups. Moreover, the $M^{II}–N_{TMTACN}$ bond distances trans to the O═P groups are lengthened in $[M^{II}(OH)Fe^{III}]^{+}$ (2.144(5)–2.257(2) Å), in comparison with those reported for the MST analogues (2.102(2)–2.164 (3) Å).[46] These observations are consistent with stronger trans influence in the $[poat]^{3-}$ system, in which the O═P donors form stronger M^{II}–O═P bonds that cause a weakening and lengthening the $M^{II}–N_{TMTACN}$ bonds.

The remaining phosphinic amido tripodal arm that does not coordinate to the M^{II} ion participates in an intramolecular H-bond with the bridging hydroxido group; the O1…O2 distances range from 2.641(2) to 2.655(5) Å, which are indicative of H-bonds and consistent with the observation obtained from FTIR spectroscopy. The O…O distances found in

$[M^{II}(OH)Fe^{III}]^+$ are comparable with those found in the $[(TMTACN)M^{II}–(\mu\text{-}OH)–Fe^{III}MST]^+$ complexes (2.619(4)–2.644(3) Å).[46]

Electrochemical properties of $[M^{II}(OH)Fe^{III}]^+$ complexes

The electrochemical properties of the $[M^{II}(OH)Fe^{III}]^+$ series were investigated using cyclic voltammetry. The $[Zn^{II}(OH)Fe^{III}]^+$ complex exhibited a reversible one-electron redox event at −1.62 V *vs.* $[FeCp_2]^{+/0}$ (i_{pc}/i_{pa} = 1.01, ΔE = 0.20 V, $\Delta E([FeCp_2]^{+/0})$ = 0.18 V) that is assigned to the $Zn^{II}Fe^{III}/Zn^{II}Fe^{II}$ couple (Fig. 6A). The $[Cu^{II}(OH)Fe^{III}]^+$ complex exhibited complex redox behavior, with a single reduction and oxidation events at −1.76 V and −1.13 V, respectively (Fig. 6B). One possible explanation for this electrochemical behavior is that the Cu^{II} center has a similar reduction potential, which likely results in a large structural change that could influence the reversibility of an electrochemical event.

The $[Ni^{II}(OH)Fe^{III}]^+$ complex exhibited a reversible one-electron redox event at −1.71 V *vs.* $[FeCp_2]^{+/0}$ (i_{pc}/i_{pa} = 1.07, ΔE = 0.18 V, $\Delta E([FeCp_2]^{+/0})$ = 0.17 V) that is assigned to the $Ni^{II}Fe^{III}/Ni^{II}Fe^{II}$ couple (Fig. 6C). The reduction potentials of the $[M^{II}(OH)Fe^{III}]^+$ complexes are significantly more negative than their $[(TMTACN)M^{II}–(\mu\text{-}OH)–Fe^{III}MST]^+$ analogs. For instance, the potential for the $[Zn^{II}(OH)Fe^{III}]^+$ complex is more negative by 0.73 V than that found for the same process in $[(TMTACN)\ Zn^{II}–(\mu\text{-}OH)–Fe^{III}MST]^+$ (−0.89 V).[46] The observed difference between the two systems is again consistent with $[poat]^{3-}$ being a stronger donating ligand than $[MST]^{3-}$, and highlights the ability of phosphinic amido groups to stabilize higher valent metal centers.[48]

Electron paramagnetic resonance properties of $[M^{II}(OH)Fe^{III}]^+$ complexes

The $[Zn^{II}(OH)Fe^{III}]^+$ complex showed signals (Fig. 7A) from an S = 5/2 species in perpendicular mode, with g = 4.96 and 3.82 arising from the M_s = ±3/2 doublet and weaker resonances at g = 9.85 and 9.15 from the M_s = ±5/2 and ±1/2 doublets, respectively. The simulation indicated D = −1.7 cm^{-1} and E/D = 0.21. The spin concentration (5 mM) determined from simulation was within error equal to that determined by the weight of the added complex. The electronic properties of this complex are comparable to that of $[(TMTACN)Zn^{II}–(\mu\text{-}OH)–Fe^{III}MST]^+$ (D = −2.5 cm^{-1}, E/D = 0.21).

The $[Cu^{II}(OH)Fe^{III}]^+$ complex showed a signal (Fig. 7B) from the S = 2 system of the antiferromagnetically exchange-coupled S = 1/2 (Cu^{II}) and S = 5/2 (Fe^{III}) ions.[46,48] The inset shows the temperature dependence of the signal intensity and a theoretical curve for the exchange-coupled spin system with J = 25 cm^{-1} and D_{Fe} = −1.7 cm^{-1}. The simulation overlaid on the spectrum assumes an S = 2 spin Hamiltonian with D = −2.3 cm^{-1}, E/D = 0.15, g_z = 2. The conversions from the uncoupled site parameters to an S = 2 system parameters are: $D = 4/3D_{Fe}$, $g_z = 2 - \Delta g_{z,Cu}/6$ and $A_z = 1/6A_{z,cu}$. For Cu^{II}, $g_{z,Cu} \approx 2.2$,[52] and $\Delta g_{z,Cu} = g_{z,Cu} - 2 \approx 0.2$, giving $g_z \approx 2$. The significant reduction of the system A_z value is cause by spin coupling that renders the Cu hyperfine unresolvable. The value of J is the same as that observed for the MST analog.

The $[Ni^{II}(OH)Fe^{III}]^+$ complex showed signals (Fig. 7C) from the S = 3/2 system of the antiferromagnetically exchange-coupled S = 1 (Ni^{II}) and S = 5/2 (Fe^{III}) ions. The signals at g = 4.99, 2.46, 1.70 are from the M_s = ±1/2 doublet and g = 5.46, 1.32 are from the M_s =

±3/2 doublet. The simulation overlaid on the spectrum uses $J = 35\ cm^{-1}$, $D_{Fe} = -1.7\ cm^{-1}$, $E/D_{Fe} = 0.21$, $D_{Ni} = +12\ cm^{-1}$, $E/D_{Ni} = 0.11$, $g_{Ni} = (2.24, 2.17, 2.18)$. All these values are comparable to the MST analog. The spin concentration (5 mM) determined from simulation was within error equal to that determined by the weight of the added complex.

Conclusions

We have demonstrated the stepwise assembly of heterobimetallic complexes from the Fe^{III}–OH synthon, $[Fe^{III}poat(OH)]^-$, and $[M^{II}(TMTACN)(OTf)_2]$. The assembly yielded $[Fe^{III}–(\mu\text{-}OH)–M^{II}]^+$ complexes in high purity, and we did not observe any unwanted side-reactions, such as scrambling of the metal ions or redox processes, which we attribute to the properties of the $[poat]^{3-}$ ligand. It provides a trianionic binding pocket that stabilizes the Fe^{III} center, while the P═O units are positioned to assist in the binding of the Ni^{II}, Cu^{II}, and Zn^{II} complexes. Spectroscopic and structural studies confirm that the metal centers have different primary coordination spheres with the Fe^{III} being five-coordinated and the M^{II} being six-coordinated. Moreover, our findings show that each complex contains an $[Fe^{III}–(\mu\text{-}OH)–M^{II}]$ core structure that persists in both solution and solid states. Results from XRD and vibrational measurements indicate that each complex contains an intramolecular H-bond between the hydroxido ligand and a P═O moiety from one of the phosphinic amido groups.

The formation of bimetallic complexes with a bridging hydroxido ligand has relevance to active sites within metalloproteins.[9-12,54] The diverse examples that have these types of core structures include the di-Fe centers in the respiratory protein hemerythrin that also contain one five- and one six-coordinate site,[7] and the FeZn site in purple acid phosphatase that degrades organophosphates.[8] The isolation of the $[(TMTACN)M^{II}–(\mu\text{-}OH)–Fe^{III}poat]^+$ complex further allowed comparisons to the related series of complexes, $[(TMTACN)\ M^{II}–(\mu\text{-}OH)–Fe^{III}MST]^+$, that are made with a sulfonamido tripod. We found major differences in the one-electron reduction potentials between these two sets of bimetallic complexes with those prepared with $[poat]^{3-}$ having significantly lower potentials. This finding indicates that phosphinic amido donors create stronger ligand fields than comparable sulfonamido donors. In addition, the $M^{II}–O_{P=O}$ bonds are shorter than the analogous $M^{II}–O_{S=O}$ which suggests that the P═O units, with their larger dipole, can form stronger M–O bonds. These results suggest that ligands with phosphinic amido groups could stabilize higher valent bimetallic complexes. We pointed out that one limitation of complexes with sulfonamido tripods is the inability to access higher valent metal centers. Tripodal ligands with phosphinic amido donors should help correct this deficiency because our data indicates that $[poat]^{3-}$ is better at stabilizing higher oxidized metal centers than the corresponding sulfonamido ligand. Our recent detection of the Fe^{IV}═O complex $[Fe^{IV}poat(O)]^-$ supports this premise and, taken together with the work presented here, illustrates the versatility and promise of this type of ligand.[48]

Experimental

General procedures

All reagents were purchased from commercial sources and used as received unless otherwise noted. Solvents were sparged with argon and purified using a JC Meyer Co. solvent

purification system with columns containing Q-5 and molecular sieves. Potassium hydride (KH) as a 30% dispersion in mineral oil was filtered with a medium porosity glass frit and washed 5 times each with pentane and diethyl ether (Et_2O). Solid KH was dried under vacuum and stored under an inert atmosphere. All synthetic manipulations were conducted in a Vacuum Atmosphere, Co. drybox under an argon atmosphere. H_3poat,[48] TMTACN,[55,56] $Zn^{II}(OTf)_2{\cdot}2CH_3CN$,[57] $[Cu^{II}(TMTACN)(OTf)_2]{\cdot}CH_3CN$,[52] and $Ni^{II}(OTf)_2{\cdot}5CH_3CN$[57] were synthesized according to previous reports.

Physical methods

Electronic absorbance spectra were recorded with a Cary 50 spectrophotometer using a 1.00 cm quartz cuvette. High resolution mass spectra were collected using Waters Micromass LCT Premier Mass Spectrometer. Solid-state Fourier transform infrared (FTIR) spectra were collected on a Thermo Scientific Nicolet iS5 FT-IR spectrometer equipped with an iD5 ATR accessory. Cyclic voltammetry experiments were conducted using a CHI600G electrochemical analyzer. A 2.0 mm glassy carbon electrode was used as the working electrode at scan velocities between 0.01 and 0.5 V s^{-1}. A ferrocenium/ferrocene ($[FeCp_2]^{+/0}$) standard was used as an internal reference to monitor the reference electrode (Ag^+/Ag). Tetrabutylammonium hexafluorophosphate (TBAP) was used as the supporting electrolyte at a concentration of 0.1 M. Elemental analyses were performed on a PerkinElmer 2400 Series II CHNS elemental analyzer. X-band EPR spectra were recorded on a Bruker ELEXSYS spectrometer equipped with an Oxford ESR-910 liquid helium cryostat and a Bruker bimodal cavity for the generation of microwave fields parallel and transverse to the applied magnetic field. The microwave frequency was calibrated with a frequency counter, and the magnetic field was measured with an NMR gaussmeter. The sample temperature was calibrated against a calibrated cernox sensor (Lakeshore CX-1050) mounted inside an EPR tube. A modulation frequency of 100 kHz was used for all EPR spectra. The simulation software SpinCount was written by one of the authors.[58] The software diagonalizes the electronic terms of the spin Hamiltonian, and performs least-squares fitting of simulations to the spectra. The quantitative simulations are generated with consideration of all intensity factors, which allows the computation of simulated spectra for a specified sample concentration. The quantification of all signals was performed relative to a CuEDTA spin standard prepared from a copper atomic absorption standard (Sigma-Aldrich). Additional information for EPR data analysis and crystallographic details are summarized in ESI.†

Synthesis of $K[Fe^{III}poat(OH)]$

Route 1 – oxygenation of $K[Fe^{II}poat]$.—$K[Fe^{II}poat]$ was synthesized *in situ* as described in the reported procedure.[48] To a solution of H_3poat (400 mg, 0.536 mmol) in anhydrous THF (13 mL) was added KH (68.0 mg, 1.64 mmol), and the reaction was allowed to proceed until gas evolution ceased and all solids were dissolved. To the solution was added $Fe^{II}(OAc)_2$ (96 mg, 0.56 mmol). The yellow solution was stirred for 25 min and then filtered through a medium fritted glass funnel to remove insoluble material. The yellow filtrate was transferred to a 50 mL Schlenk flask, which was sealed with a rubber septum and brought out from the glove box. Anhydrous O_2 (12 mL, T = 298 K, P = 1 atm, 0.54 mmol) was injected into the headspace *via* syringe. The initial yellow solution turned dark

brown and stirred for 1 h. After the reaction was complete, all volatiles were removed under vacuum, and the reaction flask was brought into the glovebox. The residues were redissolved in CH_2Cl_2 (6 mL) and were layered with Et_2O to afford dark yellow crystals (160 mg, 35%).

Route 2 – chemical oxidation of $K_2[Fe^{II}poat(OH)]$.—$K_2[Fe^{II}poat(OH)]$ was first synthesized *in situ*. To a solution of H_3poat (200 mg, 0.268 mmol) in anhydrous THF (6 mL) was added KH (33 mg, 0.82 mmol), and the reaction was allowed to proceed until gas evolution ceased and all solids were dissolved. To the solution was added $Fe^{II}(OAc)_2$ (48 mg, 0.28 mmol). The yellow solution was stirred for 25 minutes and H_2O (5 μL, 0.3 mmol) was added *via* syringe. After 5 min, the reaction mixture was filtered through a medium porosity glass frit to remove insoluble material. KH (11 mg, 0.27 mmol) was added to the filtrate, which turned orange and was allowed to stir for 10 min. The reaction mixture was then filtered through a medium porosity glass frit to remove any insoluble material. 0.5 equivalent of I_2 (34 mg, 0.13 mmol) was added to the orange solution, which turned yellow brown and stirred for 30 min. The reaction mixture was then reduced to dryness and triturated with Et_2O until the residue was a free-flowing powder. The powder was redissolved in MeCN and filtered to remove KI. Et_2O was allowed to diffuse into the MeCN solution resulting in dark yellow crystals (46 mg, 20%). Elemental analysis calcd for $K[Fe^{III}poat(OH)]\cdot(CH_3CN)\cdot(H_2O)$, $C_{42}H_{43}FeKN_4O_4P_3\cdot(CH_3CN)\cdot(H_2O)$; C, 57.77; H, 5.29; N, 7.66%, found: C, 57.74; H, 5.09; N, 7.32%. FTIR (diamond ATR, cm^{-1}): 3562, 3068, 3051, 3006, 2972, 2945, 2931, 2897, 2848, 2839, 1591, 1572, 1481, 1458, 1446, 1435, 1400, 1373, 1346, 1336, 1302, 1281, 1255, 1190, 1176, 1161, 1107, 1092, 1068, 1041, 1028, 999, 958, 924, 852, 787, 750, 735, 715, 696, 619, 579, 559, 532. EPR (X-band, ⊥-mode, DMF : THF with 2 equiv. 18-crown-6, 12 K): g = 9.6, 4.3. Mössbauer (DMF : THF with 2 equiv. 18-crown-6, 4.2 K): δ = 0.32 mm s^{-1}; ΔE_Q = 0.92 mm s^{-1}. UV-vis λ_{max}(DMF : THF with 2 equiv. 18-crown-6)/nm (ε/M^{-1} cm^{-1}): 370 (3800).

Synthesis of $[Zn^{II}(TMTACN)(OTf)_2]$

$Zn^{II}(OTf)_2\cdot 2CH_3CN$ (104.7 mg, 0.2350 mmol) was suspended in 20 mL CH_2Cl_2, and TMTACN (46.0 μL, 40.7 mg, 0.237 mmol) was added in one portion using a syringe. The reaction mixture turned clear and was allowed to react for 2 h. The solution was filtered with a fine porosity glass frit to remove any insoluble materials, and all volatiles were removed under vacuum. The white residue was redissolved in 2 mL CH_2Cl_2, and white solids were precipitated after the addition of 20 mL Et_2O. The white solids were collected on a fine porosity glass frit and dried under vacuum, affording the product (115 mg, 91.5%). Elemental analysis calcd for $[Zn^{II}(TMTACN)(OTf)_2]$, $C_{11}H_{21}F_6N_3O_6S_2Zn$: C, 24.70; H, 3.96; N, 7.86%, found: C, 24.86; H, 3.98; N, 7.66%.

Synthesis of $[(TMTACN)Zn^{II}–(\mu\text{-}OH)–Fe^{III}poat]OTf$

$K[Fe^{III}poat(OH)]$ (92.4 mg, 0.108 mmol) was dissolved in 4 mL anhydrous CH_2Cl_2. NMe_4OAc (15.6 mg, 0.117 mmol) was added in one portion, and the mixture was allowed to stir for 1 h. The reaction mixture was filtered with a fine porosity glass frit, and the filtrate was added dropwise to a 1 mL CH_2Cl_2 solution of $[Zn^{II}(TMTACN)(OTf)_2]$ (58.2 mg, 0.109 mmol). The reaction was allowed to proceed for 1 h, and the mixture was filtered with a medium porosity glass frit to remove any insoluble materials. The filtrate was layered

with Et_2O to yield a light brown powder. After the light brown powder was collected and dried, it was redissolved in CH_2Cl_2, and was layered with pentane to yield yellow sheet-like crystals. The crystals were collected on a glass frit and dried under vacuum, affording the product in yields that ranged from 40–50%. Elemental analysis calcd for [(TMTACN)Zn^{II}–(μ-OH)–Fe^{III}poat] OTf·1.5CH_2Cl_2, $C_{52}H_{64}F_3FeN_7O_7P_3SZn$·1.5$CH_2Cl_2$; C, 48.33; H, 5.08; N, 7.37%, found: C, 48.64; H, 4.85; N, 7.67%. FTIR (diamond ATR, cm^{-1}): 3141 (OH), 3074, 3049, 3020, 2993, 2964, 2947, 2902, 2877, 2848, 2817, 1591, 1493, 1483, 1464, 1435, 1363, 1267, 1223, 1165, 1140, 1115, 1084, 1065, 1030, 1016, 991, 964, 931, 891, 812, 750, 723, 696, 636. EPR (X-band, ⊥-mode, CH_2Cl_2:THF, 16 K): g = 9.85, 9.15, 4.96, 3.82. UV-vis $\lambda_{max}(CH_2Cl_2)$/nm (ε/M^{-1} cm^{-1}): 319 (4200), 372 (5200), 460 (sh). Electronspray ionization mass spectrometry (ESI-MS) (CH_3CN, ES^+, *m/z*): exact mass calcd for $[Zn^{II}(OH)Fe^{III}]^+$, $C_{51}H_{64}FeN_7O_4P_3Zn$, 1051.2875; found, 1051.2848. $E_{1/2}$ (CH_2Cl_2, V *versus* $[FeCp_2]^{+/0}$): −1.62.

Synthesis of [(TMTACN)Cu^{II}–(μ-OH)–Fe^{III}poat]OTf

This salt was prepared using the method described above for [(TMTACN)Zn^{II}–(μ-OH)–Fe^{III}poat]OTf with the following modifications: K[Fe^{III}poat(OH)] (125.7 mg, 0.1469 mmol), NMe_4OAc (21.2 mg, 0.159 mmol), [Cu^{II}(TMTACN)$(OTf)_2$]·CH_3CN (85.1 mg, 0.148 mmol). Yellow sheet-like crystals (40–50% yield) suitable for X-ray diffraction were grown from a concentrated CH_2Cl_2 solution layered with hexane. Elemental analysis calcd for [(TMTACN)Cu^{II}–(μ-OH)–Fe^{III}poat]OTf·2CH_2Cl_2, $C_{52}H_{64}CuF_3FeN_7O_7P_3S$·2$CH_2Cl_2$; C, 47.33; H, 5.00; N, 7.16%, found: C, 46.93; H, 4.88; N, 7.26%. FTIR (diamond ATR, cm^{-1}): 3053, 2987, 2962, 2900, 2858, 2821, 1589, 1491, 1483, 1469, 1441, 1435, 1360, 1263, 1223, 1173, 1149, 1134, 1115, 1068, 1030, 1014, 993, 962, 931, 893, 877, 808, 783, 752, 719, 696, 636. EPR (X-band, //-mode, CH_2Cl_2:THF, 16 K): g = 8.2. UV-vis $\lambda_{max}(CH_2Cl_2)$/nm (ε/M^{-1} cm^{-1}): 315 (sh), 372 (4200), 460 (sh). ESI-MS (CH_3CN, ES^+, *m/z*): exact mass calcd for $[Cu^{II}(OH)Fe^{III}]^+$, $C_{51}H_{64}CuFeN_7O_4P_3$, 1050.2880; found, 1050.2909. E_{pa} (CH_2Cl_2, V *versus* $[FeCp_2]^{+/0}$): −1.13. E_{pc} (CH_2Cl_2, V *versus* $[FeCp_2]^{+/0}$): −1.76.

Synthesis of [(TMTACN)Ni^{II}–(μ-OH)–Fe^{III}poat]OTf

This salt was prepared using the method described above for [(TMTACN)Zn^{II}–(μ-OH)–Fe^{III}poat]OTf with the following modifications: K[Fe^{III}poat(OH)] (190.0 mg, 0.2231 mmol), NMe_4OAc (31.2 mg, 0.238 mmol), 6 mL CH_2Cl_2. $Ni^{II}(OTf)_2$·5CH_3CN (125.9 mg, 0.2240 mmol) and TMTACN (44.0 μL, 38.9 mg, 0.227 mmol) were pre-mixed for 1 h before using. Dark yellow crystals (50–60% yield) suitable for X-ray diffraction were grown from a concentrated CH_2Cl_2 solution layered with hexane. Elemental analysis calcd for [(TMTACN)Ni^{II}–(μ-OH)–Fe^{III}poat]OTf·0.5C_5H_{12}, $C_{52}H_{64}F_3FeN_7NiO_7P_3S$·0.5$C_5H_{12}$; C, 53.15; H, 5.73; N, 7.96%, found: C, 53.15; H, 5.53; N, 7.90%. FTIR (diamond ATR, cm^{-1}): 3160 (br, OH), 3064, 3050, 3008, 2970, 2960, 2904, 2860, 2827, 1614, 1591, 1572, 1484, 1471, 1462, 1450, 1435, 1379, 1361, 1263, 1222, 1169, 1140, 1117, 1082, 1061, 1030, 1014, 991, 957, 935, 924, 897, 876, 806, 785, 750, 721, 696, 636. EPR (X-band, ⊥-mode, CH_2Cl_2: THF, 16 K): g = 5.46, 4.99, 2.46, 1.70, 1.32. UV-vis $\lambda_{max}(CH_2Cl_2)$/nm (ε/M^{-1} cm^{-1}): 312 (sh), 372 (6400), 455 (sh), 513 (sh). ESI-MS (CH_3CN, ES^+, *m/z*): exact

mass calcd for $[Ni^{II}(OH)Fe^{III}]^+$, $C_{51}H_{64}FeN_7NiO_4P_3$, 1045.2937; found, 1045.2939. $E_{1/2}$ (CH_2Cl_2, V *versus* $[FeCp_2]^{+/0}$): −1.71.

Supplementary Material

Refer to Web version on PubMed Central for supplementary material.

Acknowledgements

We thank the National Institutes of Health (GM050781 to A. S. B, and GM077387 to M. P. H.) for financial support.

Notes and references

1. Kurtz DM, Chem. Rev, 1990, 90, 585–606.
2. Wu AJ, Penner-Hahn JE and Pecoraro VL, Chem. Rev, 2004, 104, 903–938. [PubMed: 14871145]
3. Holm RH, Kennepohl P and Solomon EI, Chem. Rev, 1996, 96, 2239–2314. [PubMed: 11848828]
4. Jasniewski AJ and Que L, Chem. Rev, 2018, 118, 2554–2592. [PubMed: 29400961]
5. Greene BL, Kang G, Cui C, Bennati M, Nocera DG, Drennan c. L. and Stubbe J, Annu. Rev. Biochem, 2020, 89, 45–75. [PubMed: 32569524]
6. Martinie RJ, Blaesi EJ, Krebs C, Bollinger JM, Silakov A and Pollock CJ, J. Am. Chem. Soc, 2017, 139, 1950–1957. [PubMed: 28075562]
7. Stenkamp RE, Chem. Rev, 1994, 94, 715–726.
8. Schenk G, Mitić N, Gahan LR, Ollis DL, McGeary RP and Guddat LW, Acc. Chem. Res, 2012, 45, 1593–1603. [PubMed: 22698580]
9. Fabiane SM, Sohi MK, Wan T, Payne DJ, Bateson JH, Mitchell T and Sutton BJ, Biochemistry, 1998, 37, 12404–12411. [PubMed: 9730812]
10. Benini S, Rypniewski WR, Wilson KS, Miletti S, Ciurli S and Mangani S, Structure, 1999, 7, 205–216. [PubMed: 10368287]
11. Rosenzweig AC, Frederick CA, Lippard SJ and Nordlund P, Nature, 1993, 366, 537–543. [PubMed: 8255292]
12. Klabunde T, Eicken C, Saccettini JC and Krebs B, Nat. Struct. Biol, 1998, 5, 1084–1090. [PubMed: 9846879]
13. Kung Y and Drennan CL, Curr. Opin. Chem. Biol, 2011, 15, 276–283. [PubMed: 21130022]
14. Hsu H-F, Dong Y, Shu L, Young VG and Que L, J. Am. Chem. Soc, 1999, 121, 5230–5237.
15. Xue G, Wang D, De Hont R, Fiedler AT, Shan X, Münck E: and Que L, Proc. Natl. Acad. Sci. U. S. A, 2007, 104, 20713–20718. [PubMed: 18093922]
16. Kim K and Lippard SJ, J. Am. Chem. Soc, 1996, 118, 4914–4915.
17. Ghosh A, Tiago de Oliveira F, Yano T, Nishioka T, Beach ES, Kinoshita I, Münck E, Ryabov AD, Horwitz CP and Collins TJ, J. Am. Chem. Soc, 2005, 127, 2505–2513. [PubMed: 15725005]
18. Smith JM, Sadique AR, Cundari TR, Rodgers KR, Lukat-Rodgers G, Lachicotte RJ, Flaschenriem CJ, Vela J and Holland PL, J. Am. Chem. Soc, 2006, 128, 756–769. [PubMed: 16417365]
19. Wieghardt K, Bossek U, Nuber B, Weiss J, Bonvoisin J, Corbella M, Vitols SE and Girerd JJ, J. Am. Chem. Soc, 1988, 110, 7398–7411.
20. Dalle KE and Meyer F, Eur. J. Inorg. Chem, 2015, 3391–3405.
21. Zhao N, Filatov AS, Xie J, Hill EA, Rogachev AY and Anderson JS, J. Am. Chem. Soc, 2020, 142, 21634–21639. [PubMed: 33320644]
22. Zinn PJ, Sorrell TN, Powell DR, Day VW and Borovik AS, Inorg. Chem, 2007, 46, 10120–10132. [PubMed: 17973474]
23. Ng GK-Y, Ziller JW and Borovik AS, Chem. Commun, 2012, 48, 2546–2548.
24. Borovik AS, Papaefthymiou V, Taylor LF, Anderson OP and Que L, J. Am. Chem. Soc, 1989, 111, 6183–6195.

25. Buchanan RM, Mashuta MS, Richardson JF, Webb RJ, Oberhausen KJ, Nanny MA and Hendrickson DN, Inorg. Chem, 1990, 29, 1299–1301.
26. Blusch LK, Mitevski O, Martin-Diaconescu V, Pröpper K, Debeer S, Dechert S and Meyer F, Inorg. Chem, 2014, 53, 7876–7885. [PubMed: 25014112]
27. Peralta RA, Bortoluzzi AJ, De Souza B, Jovito R, Xavier FR, Couto RAA, Casellato A, Nome F, Dick A, Gahan LR, Schenk G, Hanson GR, De Paula FCS, Pereira-Maia EC, de P. Machado S, Severino PC, Pich C, Bortolotto T, Terenzi H, Castellano EE, Neves A and Riley MJ, Inorg. Chem, 2010, 49, 11421–11438. [PubMed: 21080710]
28. Rosenkoetter KE, Ziller JW and Heyduk AF, Inorg. Chem, 2016, 55, 6794–6798. [PubMed: 27300501]
29. Wojnar MK, Ziller JW and Heyduk AF, Eur. J. Inorg. Chem, 2017, 5571–5575.
30. Chantarojsiri T, Reath AH and Yang JY, Angew. Chem., Int. Ed, 2018, 57, 14037–14042.
31. Delgado M, Ziegler JM, Seda T, Zakharov LN and Gilbertson JD, Inorg. Chem, 2016, 55, 555–557. [PubMed: 26692111]
32. Brazzolotto D, Gennari M, Queyriaux N, Simmons TR, Pécaut J, Demeshko S, Meyer F, Orio M, Artero V and Duboc C, Nat. Chem, 2016, 8, 1054–1060. [PubMed: 27768098]
33. Pearson TJ, Fataftah MS and Freedman DE, Chem. Commun, 2016, 52, 11394–11397.
34. Coste SC, Vlaisavljevich B and Freedman DE, Inorg. Chem, 2017, 56, 8195–8202. [PubMed: 28661134]
35. Gu NX, Ung G and Peters JC, Chem. Commun, 2019, 55, 5363–5366.
36. Fajardo J and Peters JC, Inorg. Chem, 2021, 60, 1220–1227. [PubMed: 33410667]
37. Krogman JP and Thomas CM, Chem. Commun, 2014, 50, 5115–5127.
38. Greer SM, McKay J, Gramigna KM, Thomas CM, Stoian SA and Hill S, Inorg. Chem, 2018, 57, 5870–5878. [PubMed: 29708752]
39. Zhang H, Hatzis GP, Moore CE, Dickie DA, Bezpalko MW, Foxman BM and Thomas CM, J. Am. Chem. Soc, 2019, 141, 9516–9520. [PubMed: 31184140]
40. Eisenhart RJ, Clouston LJ and Lu CC, Acc. Chem. Res, 2015, 48, 2885–2894. [PubMed: 26492331]
41. Cammarota RC, Clouston LJ and Lu CC, Coord. Chem. Rev, 2017, 334, 100–111.
42. Moore JT, Chatterjee S, Tarrago M, Clouston LJ, Sproules S, Bill E, Bernales V, Gagliardi L, Ye S, Lancaster KM and Lu CC, Inorg. Chem, 2019, 58, 6199–6214. [PubMed: 30957996]
43. Cook SA and Borovik AS, Acc. Chem. Res, 2015, 48, 2407–2414. [PubMed: 26181849]
44. Schwarz AD, Herbert KR, Paniagua C and Mountford P, Organometallics, 2010, 29, 4171–4188.
45. Park YJ, Cook SA, Sickerman NS, Sano Y, Ziller JW and Borovik AS, Chem. Sci, 2013, 4, 717–726. [PubMed: 24058726]
46. Sano Y, Lau N, Weitz AC, Ziller JW, Hendrich MP and Borovik AS, Inorg. Chem, 2017, 56, 14118–14128. [PubMed: 29112385]
47. Lau N, Sano Y, Ziller JW and Borovik AS, Dalton Trans., 2018, 47, 12362–12372. [PubMed: 30118133]
48. Oswald VF, Lee JL, Biswas S, Weitz AC, Mittra K, Fan R, Li J, Zhao J, Hu MY, Alp EE, Bominaar EL, Guo Y, Green MT, Hendrich MP and Borovik AS, J. Am. Chem. Soc, 2020, 142, 11804–11817. [PubMed: 32489096]
49. MacBeth CE, Hammes BS, Young VG and Borovik AS, Inorg. Chem, 2001, 40, 4733–4741.
50. Mukherjee J, Lucas RL, Zart MK, Powell DR, Day VW and Borovik AS, Inorg. Chem, 2008, 47, 5780–5786. [PubMed: 18498155]
51. Cook SA, Ziller JW and Borovik AS, Inorg. Chem, 2014, 53, 11029–11035. [PubMed: 25264932]
52. Yang L and Tolman WB, J. Biol. Inorg. Chem, 2012, 17, 285–291. [PubMed: 21960257]
53. Perrin DD, Dissociation Constant of Inorganic Acids and Bases in Aqueous Solution, Pergamon, New York, NY, 1982.
54. Kwak Y, Jiang W, Dassama LMK, Park K, Bell CB, Liu LV, Wong SD, Saito M, Kobayashi Y, Kitao S, Seto M, Yoda Y, Alp EE, Zhao J, Bollinger JM, Krebs C and Solomon EI, J. Am. Chem. Soc, 2013, 135, 17573–17584. [PubMed: 24131208]

55. Schoenfeldt NJ, Ni Z, Korinda AW, Meyer RJ and Notestein JM, J. Am. Chem. Soc, 2011, 133, 18684–18695. [PubMed: 21970696]
56. Cao R, Müller P and Lippard SJ, J. Am. Chem. Soc, 2010, 132, 17366–17369. [PubMed: 21090678]
57. Heintz RA, Smith JA, Szalay PS, Weisgerber A and Dunbar KR, Inorg. Synth, 2002, 33, 75–83.
58. Petasis DT and Hendrich MP, Methods Enzymol., 2015, 563, 171–208. [PubMed: 26478486]

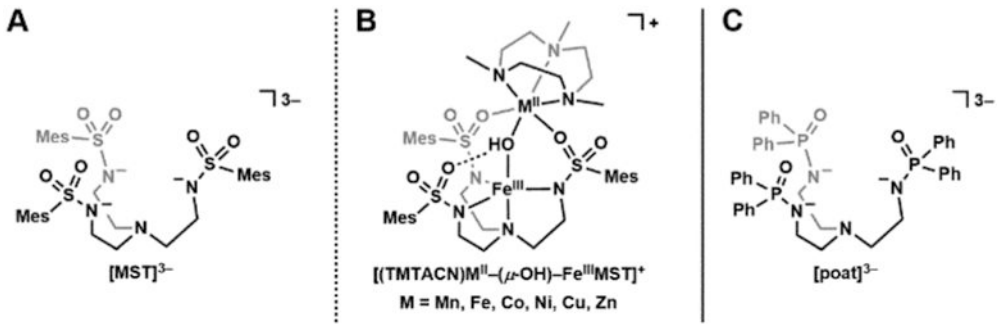

Fig. 1.
Structures of $[MST]^{3-}$ (A), $[(TMTACN)M^{II}–(\mu\text{-}OH)–Fe^{III}MST]^{+}$ (B), and $[poat]^{3-}$ (C).

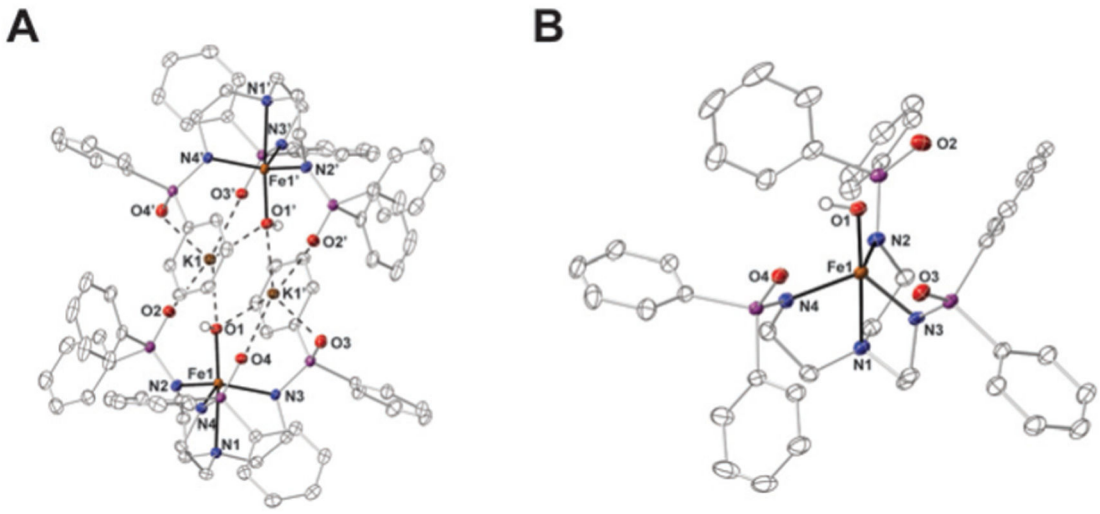

Fig. 2.

Thermal ellipsoid diagrams depicting the molecular structure of $\{K[Fe^{III}poat(OH)]\}_2$ by X-ray diffraction (A). The $[Fe^{III}poat(OH)]^-$ fragment is illustrated in (B). Ellipsoids are drawn at the 50% probability level, and only the hydroxido H atoms are shown for clarity.

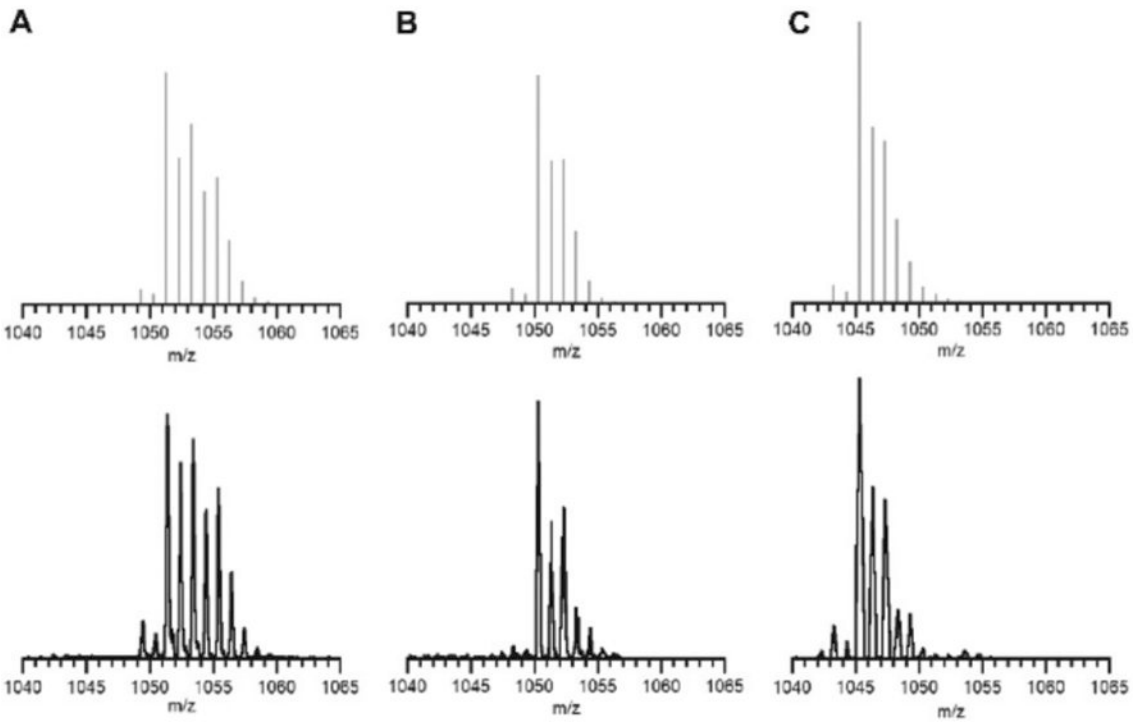

Fig. 3.

ESI-MS spectra of (A) $[Zn^{II}(O)Fe^{III}]^{+}$, (B) $[Cu^{II}(OH)Fe^{III}]^{+}$, and (C) $[Ni^{II}(OH)Fe^{III}]^{+}$, with the simulated spectra given in grey.

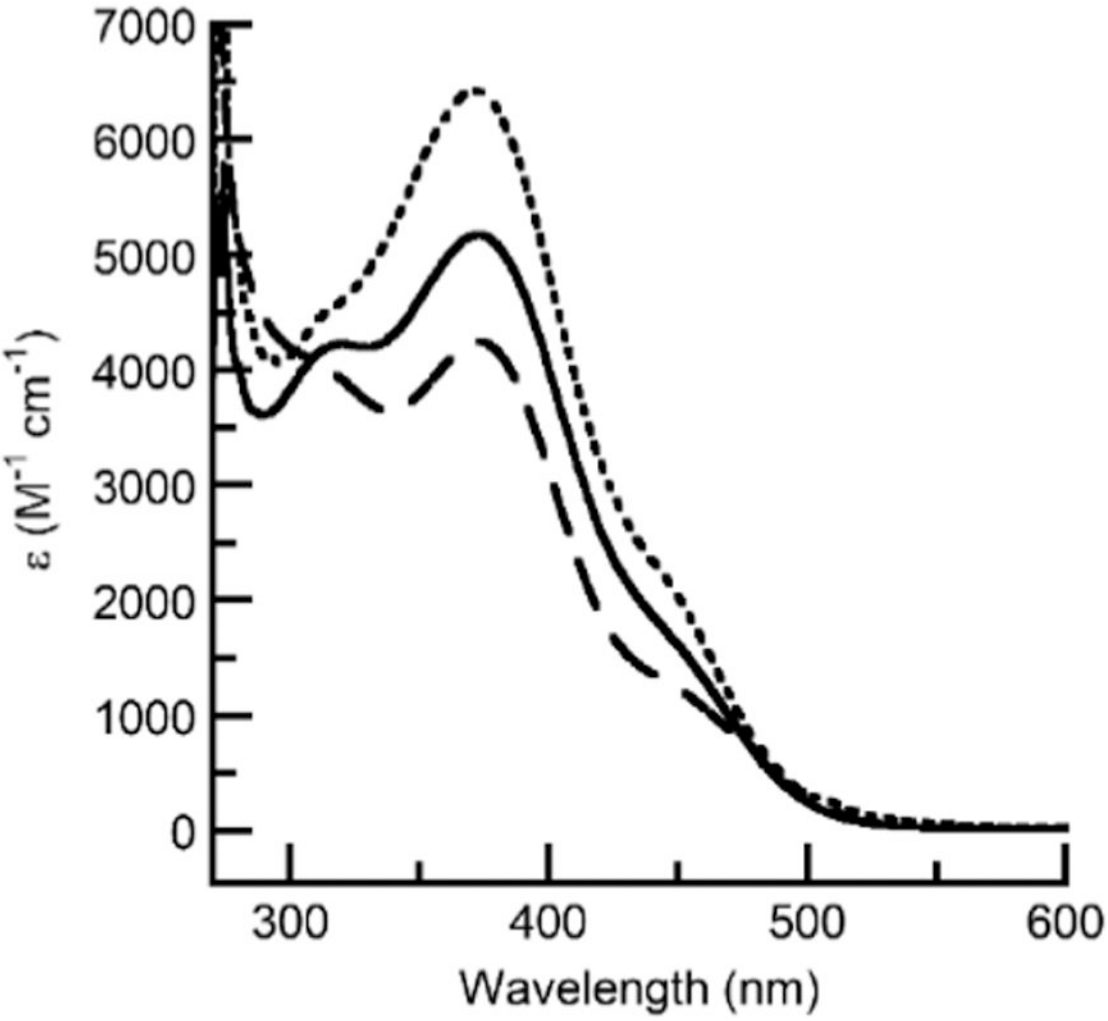

Fig. 4.

Electronic absorbance spectra for $[Zn^{II}(O)Fe^{III}]^{+}$ (black solid line), $[Cu^{II}(OH)Fe^{III}]^{+}$ (black dashed line), and $[Ni^{II}(OH)Fe^{III}]^{+}$ (black dotted line) complexes. Absorbance measurements were performed on a 0.10 mM CH_2Cl_2 solution at room temperature.

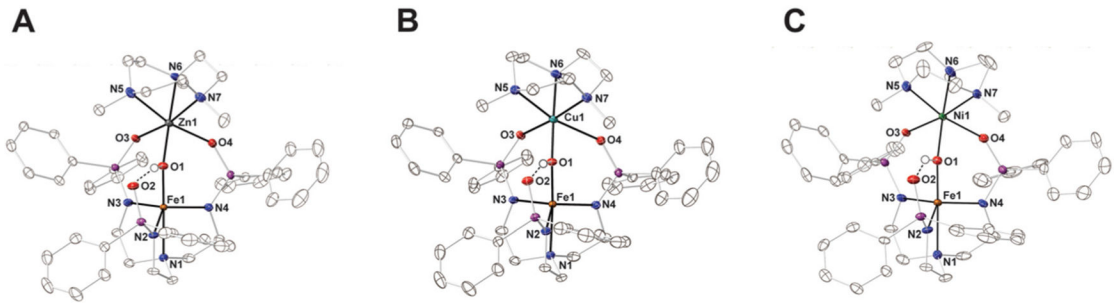

Fig. 5.

Thermal ellipsoid diagrams depicting the molecular structures of (A) $[Zn^{II}(O)Fe^{III}]^{+}$, (B) $[Cu^{II}(OH)Fe^{III}]^{+}$, and (C) $[Ni^{II}(OH)Fe^{III}]^{+}$ determined by X-ray diffraction. Ellipsoids are shown at the 50% probability level, and only the hydroxido H atoms are shown for clarity.

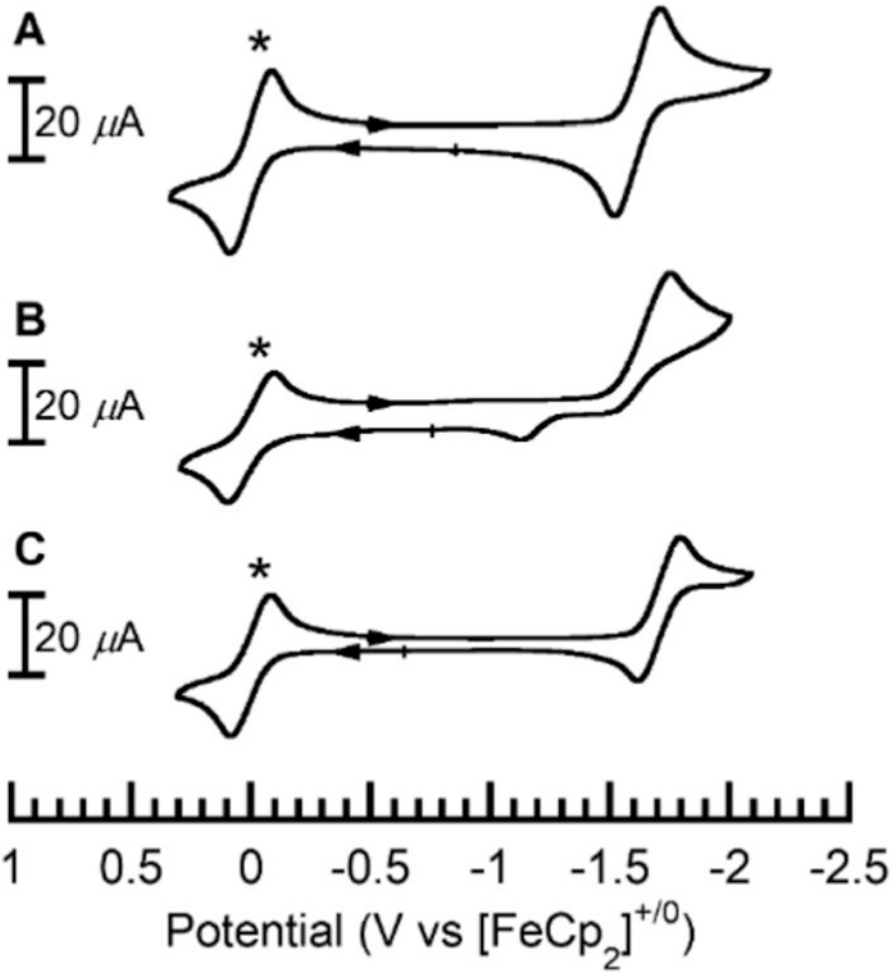

Fig. 6.

Cyclic voltammograms of (A) $[Zn^{II}(O)Fe^{III}]^{+}$, (B) $[Cu^{II}(OH)Fe^{III}]^{+}$, and (C) $[Ni^{II}(OH)Fe^{III}]^{+}$. The cyclic voltammograms were collected at 100 mV s^{-1} in the presence of $[FeCp_2]$ (*).

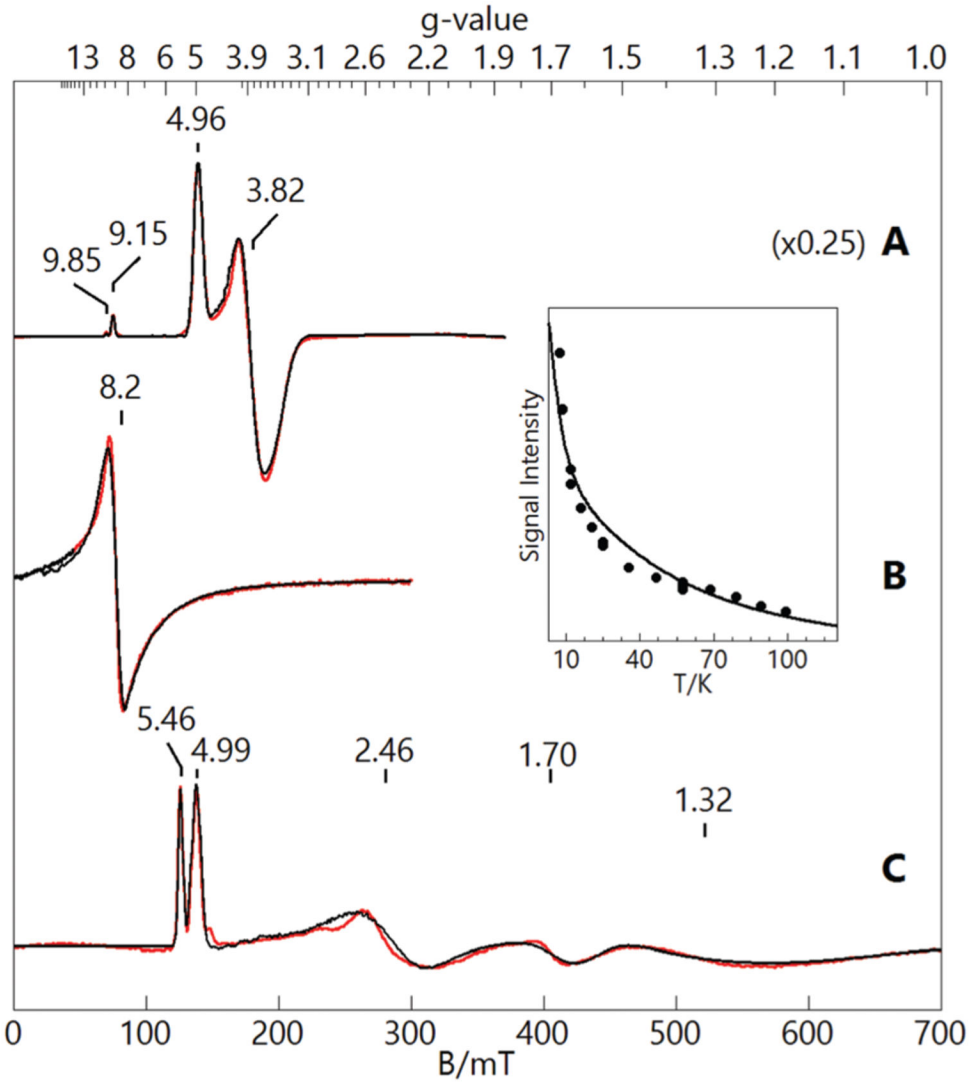

Fig. 7.

EPR spectra (red lines) and simulations (black lines) of (A) $[Zn^{II}(OH)Fe^{III}]^{+}$, (B) $[Cu^{II}(OH)Fe^{III}]^{+}$, and (C) $[Ni^{II}(OH)Fe^{III}]^{+}$. Sample concentrations: 5 mM in CH_2Cl_2 : THF. Instrumental conditions: Temperature, 16 K; microwave frequency, 9.645 GHz, $B_1 \perp B$ (A and C), 9.343 GHz, $B_1 \| B$ (B); microwave power, 0.2 mW. See text for simulation. parameters.

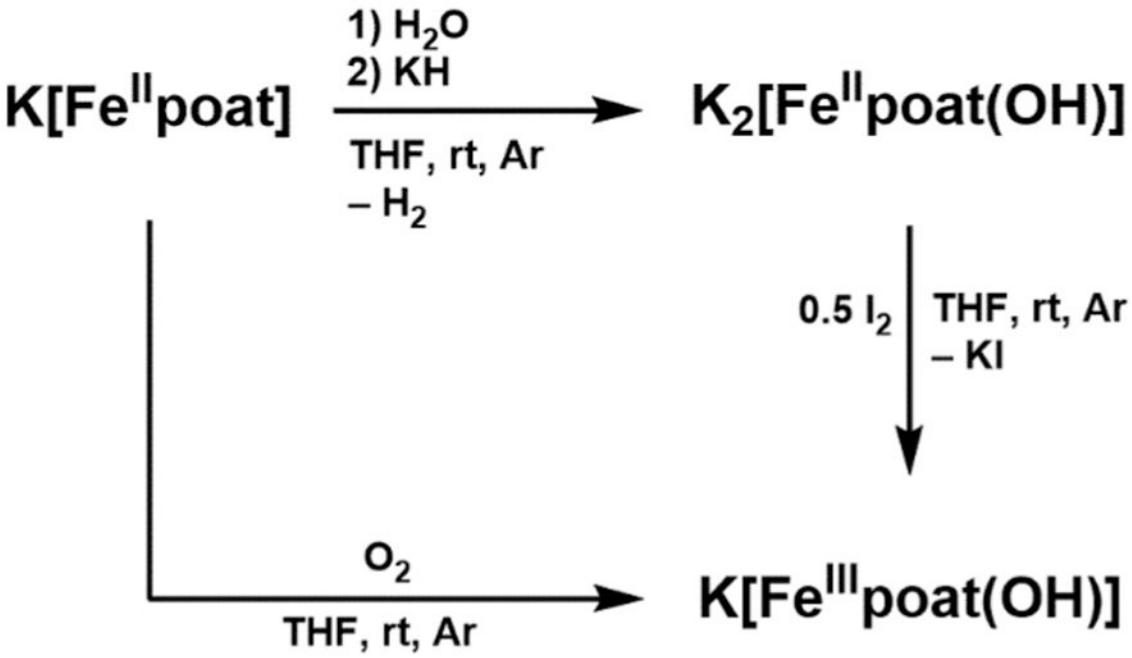

Scheme 1.
Preparative routes to the monomeric Fe–OH complexes.

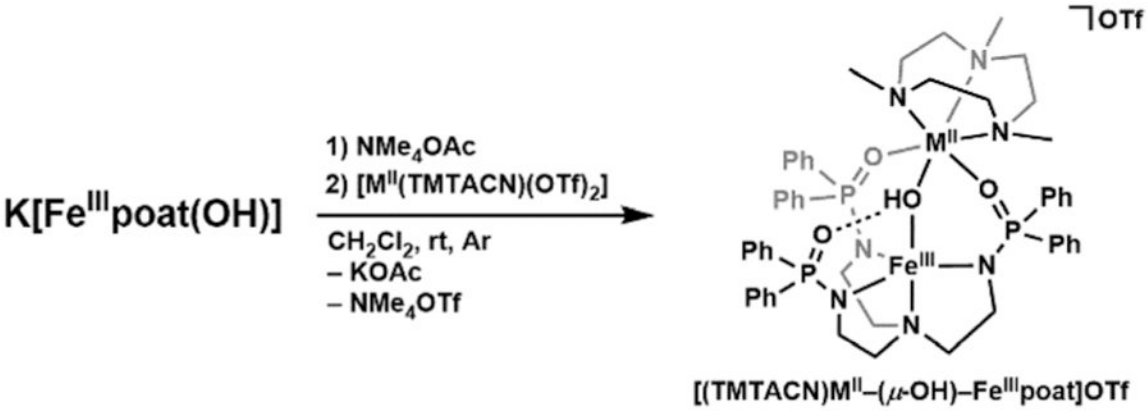

Scheme 2.
Preparative route to the bimetallic $[M^{II}(OH)Fe^{III}]^{+}$ complexes (M^{II} = Zn, Cu, Ni).

Table 1

Selected bond lengths/distances (Å) and angles (°) for $[M^{II}(OH)Fe^{III}]^{+}$ complexes[a]

	M^{II}		
$[M^{II}(OH)Fe^{III}]^{+}$	**Zn^{II}**	**Cu^{II}**	**Ni^{II}**
	Bond lengths/distances (Å)		
Fe1–N1	2.207(2)	2.205(1)	2.224(5)
Fe1–N2	2.022(2)	2.024(1)	2.017(4)
Fe1–N3	2.005(2)	1.996(1)	2.000(5)
Fe1–N4	2.007(2)	2.006(1)	2.007(5)
Fe1–O1	1.900(2)	1.898(1)	1.887(4)
O1…O2	2.653(2)	2.641(2)	2.655(5)
M1–O1	1.983(2)	1.910(1)	1.981(4)
M1–O3	2.115(2)	2.354(1)	2.091(4)
M1–O4	2.097(2)	2.019(1)	2.089(4)
M1–N5	2.240(2)	2.132(1)	2.144(5)
M1–N6	2.154(2)	2.038(1)	2.106(5)
M1–N7	2.257(2)	2.357(2)	2.156(5)
Fe1…M1	3.416(1)	3.409(1)	3.423(1)
av Fe1–N_{eq}	2.011(2)	2.009(1)	2.008(5)
av M1–N_{TMTACN}	2.217(2)	2.176(1)	2.135(5)
d[Fe1–N_{eq}]	0.364	0.360	0.370
d[M1–N_{TMTACN}]	1.474	1.405	1.370
	Angles (°)		
O1–Fe1–N1	174.54(8)	173.69(5)	174.54(17)
N2–Fe1–N3	121.44(9)	120.87(6)	121.94(20)
N3–Fe1–N4	109.64(9)	110.75(6)	108.92(20)
N2–Fe1–N4	119.26(9)	118.91(6)	119.09(19)
Fe1–O1–M1	123.26(9)	127.04(7)	124.45(20)
O3–M1–O4	96.68(7)	94.24(4)	94.46(15)
N5–M1–N6	81.31(8)	84.55(6)	84.03(18)
N5–M1–N7	78.96(8)	79.74(5)	81.99(19)
N6–M1–N7	81.35(9)	82.01(6)	83.70(20)
	Calculated values		
τ_5 [b]	0.885	0.880	0.877

[a] Bond lengths, distances, and angles are reported as an average.

[b] Trigonality structural parameter, $\tau_5 = (\beta - \alpha)/60°$. β is the largest bond angle observed, and α is the second largest bond angle observed.